Atomistic modelling of ploughing friction in silver, iron and silicon

D. Mulliah, S. D. Kenny, E. McGee and Roger Smith *,

Modelling of Materials Group, Department of Mathematical Sciences, Loughborough University, Loughborough, Leicestershire LE11 3TU, UK.

Asta Richter, B. Wolf

Department of Engineering Science, University of Applied Sciences, 15745 Wildau, Germany.

Abstract

Molecular dynamics (MD) simulations of atomic-scale stick-slip have been performed for a diamond tip in contact with the (100) surface of fcc Ag, bcc Fe, Si and H-terminated Si, at a temperature of 300 K. Simulations were carried out at different support displacements between 5 and 15 Å. The simulations illustrate the important mechanisms that take place during stick-slip. In particular, for the case of the metals they show a direct link between tip slip events and the emission of dislocations from the point of contact of the tip with the substrate. This occurs both during indentation and scratching. For the case of silicon, no slip events were observed and no sub-surface dislocations were generated underneath the scratch groove. At the deeper support displacement of 15 Å the silicon atoms undergo some local phase transformations and the atom co-ordination number varies between 5 and 8, with the majority being 5-fold or 6-fold coordinated. Both the dynamic and the static friction coefficients were found to be higher for Si compared to the corresponding values for H-terminated Si. Comparisons were made between the MD simulations and experimental measurements for indentation on the (100) surface of Si and Al. A good qualitative agreement was observed between the experimental and theoretical results. However in both the cases of Si and metals the MD simulations give a contact pressure under load that is depth dependent and values that are higher than experimental nanohardness values.

pacs : 61.72.Bb, 61.72.Ff, 68.35.Af, 68.35.Gy

Keywords: atomistic simulations, molecular dynamics, nanoidentation, mechanical properties

* Corresponding author: E-mail: R.Smith@lboro.ac.uk, Tel: +44 (0) 1509 22 3192

1 Introduction

Tribology can be defined as the science of friction, lubrication and wear [1,2]. Despite being one of the oldest applied technologies, e.g., the use of firerods by the Neanderthals dates back to 200,000 B.C with the laws of solid friction being formalised by Amontons and Coulomb almost 300 years ago [3], tribology can still be viewed as a 'young' field considering the important progress made recently. Nanotribology [4,5] which is the study of the microscopic mechanisms of tribology is an emerging research field. Solid friction results from a combination of very different processes, such as the geometric locking of two surfaces, elastic and plastic deformations, wear, lubrication, adhesion, and so on [4]. All these processes occur on very different length scales: on the nanometre scale, atomic and molecular interactions take place, whereas the largest tribological length scales are related to the stick-slip motion of tectonic plates resulting in earthquakes. The main challenge of modern tribology is to develop a fundamental understanding of solid friction, which will allow us to bridge the different length scales and properly relate the atomistic processes with the macroscopically observed phenomena.

Understanding material properties on the nanometre-scale is crucial, for example, in developing the fundamental ideas needed to design new coatings with tailor-made friction and wear properties. One of the ways to characterise these properties is through the use of the scanning force microscope (SFM). This technique is proving to be a very versatile tool that can provide information on the atomic-scale. Atomistic computer simulations are also having a major impact on this area of material science. This is largely due to recent increases in computer power, increasingly clever algorithms and recent developments in modelling interatomic interactions [5].

In this work, we consider the two main aspects of nanotribology, namely, friction, specifically ploughing friction, and wear. Our foremost interest is to investigate the stick-slip friction mechanism [6]. Bowden and Tabor attributed elastic deformation as a primary cause of macroscopic stick-slip but it is not clear whether this will also be the case for the stick-slip processes on the nanometre-scale. Atomic-scale stick-slip in an SFM was first reported by Mate *et al.* [7]. In recent years a number of theoretical and experimental investigations have been carried out to give an insight into the nanoscale stick-slip. Landman and co-workers found atomic-scale stick and slip behaviour when shearing a Si tip on a Si(111) surface [8] and a CaF_2 tip on a CaF_2 substrate [9] by using molecular dynamics (MD) simulations. Sørensen *et al.* [10] performed MD simulations and observed a transition from smooth sliding with no static friction at low loads to atomic-scale stick-slip motion at larger loads. They found that larger loads also led to slip motion and plastic deformation of the tip. Other atomistic simulation work can be found in [11–13] and ex-

perimental work in Refs. [13–15]. Most MD studies of the stick-slip have been concerned with sliding friction [10,11,16,17]. However, scratch testing is an important practical tool for the investigation of surface mechanical properties and with this in mind this investigation focuses on ploughing rather than sliding friction.

In previous work [18], we investigated the atomic-scale stick-slip phenomenon of a pyramidal diamond tip inserted into the Ag(100) surface. These simulations were all performed at low temperature. Analysis of the dynamic features of the substrate showed that dislocations underneath the scratch groove on the Ag substrate were extrinsically linked to the slip events. The current simulations are all carried out at 300 K. We also investigate the stick-slip phenomenon on materials with different crystal structures, *i.e.* face-centred cubic silver, body-centred cubic iron, and diamond silicon. Furthermore, for the Si substrate, the effect of adhesive forces with the diamond tip is investigated, and compared with the effect of hydrogen-terminating the Si surface, which passivates the dangling bonds.

2 Simulation Methodology

Fig. 1 shows a schematic representation of the model employed in the MD simulations. It illustrates the configuration of the tip and the substrate in our system. The model consists of an indenter attached to three springs, positioned in the horizontal (x), vertical (y) and lateral (z) directions. The horizontal, vertical and lateral springs are attached to support blocks A, B and C and have spring constants k_x, k_y, and k_z, respectively. This model mimics the role of the cantilever in the SFM, used for the experiments. The simulation consists of three main stages, namely, the indentation of the substrate, the relaxation of the system, which is then followed by the scratching of the substrate via the horizontal displacement of the support A.

The indenter has the configuration of a 90° triangular-based pyramid, and is constructed by taking a cubic diamond crystal with {100} faces and cutting along the diagonal (111) plane. The tip of the indenter is the vertex formed by three intersecting {100} faces and the most stable configuration is when the atoms on the three {100} planes are dimer reconstructed. Experimentally the tip is not atomically sharp and so curvature is also added to the indenter by truncating a number of atoms at the apex [18]–[24]. This adds a curvature of about 20 Å to the tip apex and reduces the apex length, see figure 1. The interaction between the indenter atoms, *i.e.* the C-C interactions are described by Brenner's many-body potential [25,26]. The indenter employed is configured from 8,432 atoms and is orientated so that the tip moves with the (111) planes parallel to the surface of the substrate.

The substrates utilised take the form of a rectangular crystal lattice and we have employed fcc silver, bcc iron, silicon and hydrogen-terminated silicon as substrates. The interactions in the metals, *i.e.* the Ag-Ag and the Fe-Fe interactions are described by the Ackland embedded atom method (EAM) potential [27] and the Finnis-Sinclair potential [28], respectively. With the Ag-C and Fe-C interactions are assumed to be purely repulsive and given by the Ziegler-Biersack-Littmark (ZBL) potential [29]. Hence, for these two cases there is no bonding between the tip and substrate. The Si-Si and Si-C interactions are modelled using the Tersoff potential [30], and therefore, we do have adhesion in this case. For this particular reason, simulations were also run with H-terminated Si to investigate any difference that strong adhesive forces might have. A combination [31] of the Brenner potential [25,26] for C-H systems, the Tersoff potential [30] for Si-C systems and the Si-H potential presented by Murty *et al.* [32], is used to model the interactions within the C-Si-H systems.

The boundary conditions imposed on both the indenter and the substrate atoms consist of fixed atoms, thermalised atoms and unconstrained atoms. The thermalised atoms are attached to the Nosé-Hoover thermostat [33,34] to control the temperature and keep the temperature of the system at 300 K. Periodic boundary conditions are applied to all vertical sides of the substrate. The fixed atoms are the outer two layers located on these vertical sides and those composing the two bottom layers. The top three layers of the indenter are also fixed and constrained to move by the vertical spring. The next three layers of the indenter and five layers of the substrate consist of thermalised atoms. The remaining atoms are unconstrained. The number of substrate atoms and the dimensions of the substrate that are employed in the simulations are given in Table 1.

Simulations were carried out at support displacements of 5 and 15 Å and at a sliding speed of $V_A = 1.0$ ms^{-1}, where V_A is the sliding speed of the horizontal support A. For the simulations performed at a depth of 5 Å, the spring constants of the horizontal, vertical and lateral springs used in the calculations were $k_x = 40.05$ Nm^{-1}, $k_y = 240.30$ Nm^{-1} and $k_z = 240.30$ Nm^{-1} respectively, whereas for the simulation at the deeper indent of 15 Å the spring constants were $k_x = 120.15$ Nm^{-1}, $k_y = 352.44$ Nm^{-1} and $k_z = 352.44$ Nm^{-1}. The mass of the tip was taken to be 3.14×10^{-23} kg. The value of the vertical spring constants were chosen to be consistent with values in an SFM device and also so that the springs did not elongate or compress excessively during a simulation.

The indenter apex is first positioned outside the range of the tip-substrate interaction potential above the substrate surface. The springs are assumed to be connected to the atoms of the top few (111) planes of the indenter. These atoms are treated as a point mass that move together and experience

an integrated vertical force F_y from all the atoms below in the indenter and also a force from the attached spring. During the indentation phase the fixed atoms are constrained in the horizontal (x) and lateral (z) directions. Thus, the equation of motion of this point mass during the indentation process is given by

$$ma_y(t) = F_y(t) + k_y\left(y_{\mathrm{B}}(t) - y(t)\right), \tag{1}$$

where $a_y(t)$ is the vertical acceleration of the indenter atoms at time t, m is the mass of the tip and $y(t)$ is the vertical displacement. The term $k_y\left(y_{\mathrm{B}}(t) - y(t)\right)$ is the spring force on the indenter. The displacement of the vertical support B, shown in Fig. 1(a), is given by $y_{\mathrm{B}}(t) = V_{\mathrm{B}}t,\ 0 \leq t \leq T_I$ and $y_{\mathrm{B}}(t) = y_{max} = V_B T_I,\ T_I < t \leq T_{rel}$. Here V_{B} is the constant velocity of the vertical support B during the indentation period, T_I is the indentation time and T_{rel} the time at which the relaxation process ends. In all cases $(T_{rel} - T_I)$ was fixed at 10 ps.

During the scratching stage, the fixed layer of indenter atoms are displaced in the horizontal (x) direction by motion of the support A. In addition the supports B and C are kept fixed in the y-direction and z-direction respectively, this allows the tip to move in these directions but imparts a restoring force. Thus, the equations of motion of the top fixed layer of the indenter atoms during the scratching phase are given by

$$ma_x(t) = F_x(t) + k_x\left(V_{\mathrm{A}}t - x(t)\right), \tag{2}$$

$$ma_y(t) = F_y(t) + k_y\left(y_{\max} - y(t)\right), \tag{3}$$

$$ma_z(t) = F_z(t) - k_z z(t). \tag{4}$$

In Eqs. [2]–[4], the forces $F_x(t)$, $F_y(t)$ and $F_z(t)$ are the integrated forces arising from the action of the other indenter atoms with the fixed top-layer atoms of the tip in the horizontal (x), vertical (y) and lateral (z) directions, respectively. $F_x(t)$ and $F_y(t)$ are defined as the frictional and normal forces at time t, respectively, and thus the friction coefficient $\mu(t) = |F_x(t)/F_y(t)|$. In the presentation of the results that follow, we define the dynamic friction coefficient (μ_k) as the time average value of $\mu(t)$ excluding the largest maxima of $\mu(t)$ which corresponds to the occurrence of slip events, and the static friction coefficient (μ_s) is calculated as the average of the largest maxima of $\mu(t)$.

In all our simulations, the classical equations of motion for all the atoms in the system were numerically integrated using the velocity-Verlet algorithm [35] with a constant timestep of 1.0 fs.

3 Experimental Methodology

Experimental investigations were carried out on the (100) surface of untreated Si and Al single crystals (Ag crystals were not available at the time). All experiments were performed with a Hysitron Triboscope attached to a Nanoscope IV scanning force microscope. The Triboscope allows indentation tests to be performed with repeated loading and unloading [36]. These intelligent load functions result in multicycling indents at the same place on the sample surface. After loading, the force is decreased to about 20 % of the load maximum. This is done to avoid losing tip-to-sample contact. The sample is then reloaded to a maximum force, which is higher than that of the previous cycle. Multicycling testing enables us to obtain hardness and elastic modulus as depth dependent data. In addition to vertical motion and indentation, the Triboscope also allows lateral motion across the surface, thus allowing scratching and material removal to be investigated.

4 Results and Discussions

The results will be presented, by making first a comparison between experimental and theoretical results during the indentation phase. Secondly, scratching simulations will be compared and contrasted for the four different substrates. During scratching we will also study whether constraining the indenter motion in the lateral (z) direction shows any significant difference compared to unconstrained motion. Finally, we will investigate the effect of temperature on the scratching process by comparing the behaviour of dislocation emission.

4.1 ***Indentation Results***

Simulations of nano-indentation has been considered previously by the authors for low temperature substrates [21,37]. Here we concentrate only on the main features of the indentation process at 300K and compare the different materials with the fcc and diamond lattice structure. We shall first discuss the results from the measurements on Al, then the investigation on Si.

4.1.1 ***Results on fcc metals***

During the indentation process the tip induces the creation of dislocations [21], and this process is dependent on the size of the indent. In the region up to 400 nm contact depth, the hardness decreases and this is observed partic-

ularly for the case of metals. Multi-indent experiments comprising of 7 cycles have been performed on single crystalline Al and Fig. 2(a) shows this hardness decrease for the Al sample with increasing load. When the penetration depth approaches a certain value, the hardness is influenced by intrinsically existing dislocations in the material. Around this zone of penetration depth the hardness reaches a plateau and is found to be no longer dependent on the contact depth. This is generally the expected constant hardness value for a material. This behaviour is seen in the depth dependent hardness curves for Al(100) (Fig. 2(a)).

Since both Al and Ag have a fcc structure and have similar hardness values, we can perform a comparison between the experiments on Al and the MD simulations on Ag. The contact pressure is defined as the ratio of the normal force and the contact area during indentation. Nanohardness is usually defined as the ratio of the normal force and the contact area after the load has been removed. For the simulations, the contact area during indentation is taken as the cross-sectional area of the indenter, which is $\left(3\sqrt{3}/2\right) b^2$, where b is the calculated indentation depth and is given by $b = h + l$, where h is the actual indenter penetration depth at peak load and l is the length that has been truncated at the apex of the indenter to give the tip a certain radius of curvature. Fig. 2(b) shows the contact pressure as a function of indentation depth for the case when nanoindentation simulation was performed on Ag at a support displacement of 15 Å. Comparing Figs. 2(a) and 2(b), we can observe that both graphs follow the same trend despite the disparate length scales. In the case of Al (Fig. 2(a)) at 500 nm, the nanohardness has reduced to the classical hardness value. In Fig. 2(b) the contact pressure for Ag has not yet reached a limiting value at the depth of 15 Å, the maximum indentation depth considered in the MD simulations. At 15 Å the calculated contact pressure is about a factor of 10 greater than the experimental hardness value for Ag.

Both the contact pressure and the hardness plotted as a function of depth in Fig. 2(b) show flat areas where the force on the tip remains constant as the depth increases. These 'pop-ins' correspond to the emission of dislocations [21]. The yielding for single crystals is often manifested by such a sudden depth excursion due to nucleation and propagation of dislocations [38,39]. Figs. 3(a)-(d) show the atomic displacements in the Ag substrate during part of the indentation. The emission shown in Fig. 3(b) and subsequent retraction of dislocations from under the tip shown in Fig. 3(c) is a fast process, occurring on the picosecond time scale at a substrate temperature of 300 K. Dislocation emission corresponds to the relief of stress during indentation.

It is often claimed that the load-depth curves obtained with pyramid indenters are parabolic hence showing a $F_y \propto h^2$ behaviour, where F_y is the normal force and h is the indentation depth. However, the nanoindentation experiments on Al demonstrates that the force-displacement curve is nearly linear. Assuming

$F_y \propto h^s$ ([23]), where s is a positive real number, the value of s can be calculated as the gradient of the line of best fit by plotting $\log F_y$ against $\log h$. The MD simulations on Ag results in $s = 1.2$. This is a lower value than found when employing the model at 0 K where no spring was involved during the nanoindentation process [23].

4.1.2 ***Investigations on Si(100)***

Due to the high cost of creating dislocations in some materials there is an extended region of pure elastic contact. At a particular depth in Al or Ag the material starts to undergo plastic deformation and dislocations are emitted, observed by the "pop-in" in the force-depth curve. Such a pop-in does not occur in all materials. Materials can, if this is energetically favourable, undergo a phase transformation. This can limit the applied pressure and as a result the hardness remains constant over a large range of load. Fig. 4(a) shows the displacement-force curve from the nanoindentation experiments on the (100) surface of untreated Si, which is an example of one such material that exhibits phase change under pressure. The multicycling indentation experiments on Si (unloading and reloading) illustrate hysteresis loops, which result from phase transformations. The experimental results give a hardness value for Si as ≈ 12 GPa, calculated from the force-displacement curve which is constant for all the depths considered and the same as the classical hardness value.

Figs. 4(b) and 4(c) give the computed force-displacement and contact pressure-displacement curves calculated from the simulations. Multi-cycling was not included in the computations due to the relatively small indentation depths and the length of time that such computations would have required. The contact pressure (under load) shows a slow reduction with depth. In this case we extended the indentation depth to 2.5 nm. Note the large pull-off force due to the attraction of the unpassivated diamond surface to the silicon evident in fig. 4(b). During indentation into Si the spring undergoes oscillations and so for clarity only the average curves have been drawn for the contact pressure. The MD simulations show that the nanohardness and scratch hardness values of Si and H-terminated Si vary less rapidly with indentation depth, compared to the metals. The energy required to create dislocations in Si is higher than the energy for phase transition. Since this phase transition occurs at a certain contact pressure, Si should not have highly depth dependent properties, which is what we can observe from the simulation results for Si in Fig. 4(c) and Table 2, where the contact pressures of Si at a depth of 5 and 15 Å are 27 and 23 GPa, respectively and for H-terminated Si, 23 and 19 GPa. Thus, the value of the contact pressure reduces only slowly for Si as the depth increases compared to very large changes for metals. These values are still about twice the experimental hardness values and are overestimated mainly because the small depths involved but it could also be influenced by the fact that the

modelled substrate is dislocation free. Fitting a curve of the form $F_y \propto h^s$ to the force-depth data as for Ag gives a higher value of s of ≈ 1.6.

4.2 ***Scratch results***

During the scratching, the indenter ploughs through the substrate resulting in the piling-up of substrate atoms in front of the indenter and along the sides of the scratch groove. The indentation depth determines the degree of pile-up in front of the indenter. The height of the pile-up in front of the indenter is given in Table 2 for the different substrates at the two depths of 5 and 15 Å. As this pile-up increases there is more resistance to motion, therefore, a greater force is required to overcome this resistance which leads to an increase in the frictional force. It can clearly be observed that both the average normal and frictional forces (see Table 3) increase with the indentation depth. This in turn has a significant influence on both the dynamic and static friction coefficients. For the cases of the metals (Ag and Fe), both the dynamic and the static friction coefficients increase with increasing indentation depth, whereas the opposite behaviour is observed for Si and H-terminated Si.

As the depth increases the tip displacement through the substrate is more difficult because there is resistance to the motion from the atoms in front of the tip. Thus, at the deeper depth the resistance to motion due to material resistance becomes more important than that due to adhesion. In addition, we can observe from Table 3 that Si and H-terminated Si have higher dynamic and static friction coefficients compared to those for the metals. Both the dynamic and static friction coefficients of Si are higher than the friction coefficients for H-terminated Si, which would also indicate an adhesion effect, particularly because as the indentation depth increases both the dynamic and static friction coefficients were found to lie closer together. This is illustrated in Figs. 5(a) and 5(b).

For the case of Ag the dynamic and static friction coefficients $\mu_k = 0.37$ and $\mu_s = 0.51$ for the vertical support displacement of 15 Å, corresponding to an actual tip depth of 10.7 Å, are similar to those obtained from the simulations at 0 K ($\mu_k = 0.43$ and $\mu_s = 0.50$).

4.2.1 ***Effect of substrate structure: Metals v/s Si v/s H-terminated Si***

Two parameters that have been calculated from the MD simulations are the contact pressure and the scratch hardness. The scratch hardness of the substrate is defined as the ratio of the average normal force during the scratching and the area supporting the indenter, kw^2, where w is the scratch width [40]

and k is a geometrical factor which depends on the tip shape. The nanohardness and scratch hardness values for the different substrates employed in the simulations are given in Table 2. The contact pressure is higher than the scratch hardness for all the substrates, see Table 2 but the trend diminishes with increasing depth.

Figs. 6(a)–6(d) give a comparison between the scratches on the Ag, Fe, Si, and H-terminated Si substrates at a depth of 15 Å. Figs. 6(e)–6(f) show experimental results with deeper depths of ≈100 nm for Al and ≈30 nm for Si and longer scratches than the simulations. We can see that unlike the Ag and the Fe substrates, there is no pile-up at the beginning of, or along the scratch for the case of Si and H-terminated Si. The experimental results also show only a small pile-up along the scratch for Si with a more extended pile-up for the fcc metal, despite the length scale disparity between the experimental and simulation results.

Fig. 7(a) shows that at the beginning of the scratching simulations on Si and H-terminated Si at the depth of 15 Å, the indenter undergoes a vertical displacement and thus indents further into the substrate, while it moves slightly in the negative z-direction, Fig. 7(b). Figs. 7(a) and 7(b) show that at the point where the tip undergoes a maximum displacement in both the y and z directions, the indenter starts rising upward toward the substrate surface and in the positive z-direction. Figs. 7(c) and 7(d) show the behaviour of the vertical and lateral spring forces, respectively. At this point the vertical spring force decreases whereas the lateral spring force increases.

The alternation between the stick and sliding states of the system reflects changes in the way energy is stored. While the tip sticks, elastic energy is stored as potential energy due to the work done by the horizontal support A. When the system slips this elastic energy is released into kinetic energy and eventually dissipated as heat. The system then sticks once more, begins to store elastic energy, and the process continues. However this exchange between kinetic and potential energy is only apparent for the results of the metal substrates. Figs. 8(a)–8(h) illustrate the trend of the potential energy of the system during the scratching simulation at a depth of 15 Å, for the different substrates employed in our simulations.

The pure Si substrate shows an initial decrease in potential energy due to bonds forming between the tip and the substrate. For the small depths considered the pull-off force is of the same order of magnitude as the compressive force during, see figure 4b. However there are no stick-slip events discernible from either the Si or H-Si surfaces. Figs. 8(f) and 8(h) show that for both Si and H-terminated Si there is a gradual increase in the potential energy during the scratching simulations, except that at the beginning of the scratching simulation on Si. This gradual increase is due to partial amorphisation where

atoms displaced from their equilibrium positions cannot overcome the energy barriers to return to their preferred diamond lattice sites. As scratching proceeds, bonds between some of the C atoms of the tip and the substrate atoms at the rear of the indenter are broken, while new bonds are formed between some of the C atoms and Si atoms in front of the indenter. Figs. 6(c) and 6(d) show attachment of Si atoms to the rear of the tip for the Si and H-terminated Si surfaces. The reduced adhesion force for the H-terminated Si case is responsible for a reduced friction coefficient compared to the bare Si surface.

The dislocation emission is illustrated in Figs. 9(a)–9(f) and Figs. 10(a)–10(f) for Ag and Fe, respectively. Here the atoms are represented as spheres and are shaded according to the modulus of the slip vector [41,42]. Figs. 9(a)–9(f) can be compared directly to Fig. 10(a), where the slip events during the scratching simulation on Ag are indicated by the arrows. During the occurrence of the slip event around $t = 1.0$ ns there is the emission of a first dislocation, followed by the emission of a second dislocation and the retraction of the first one. Here, the red atoms show the region of the Ag lattice that have undergone a perfect dislocation, with Burgers' vector $\mathbf{b} = \frac{1}{2}\langle 110\rangle$. The green atoms designate those atoms that are on a stacking fault and the boundary in the plane of the fault, separating the faulted region from the perfect region of the Ag lattice, is a Shockley partial dislocation, with Burgers' vector $\mathbf{b} = \frac{1}{2}\langle 112\rangle$. As expected, an fcc material slip is observed to occur on the $\{111\}$ planes with slip occuring in $\langle 110\rangle$ directions. Moreover, the emission and retraction of a dislocation occurs over a very short time scale.

For the case of Fe, shown in Figs. 10(a)–10(f) the red atoms show the region of the Fe lattice that have undergone a perfect dislocation with Burgers' vector $\mathbf{b} = \frac{1}{2}\langle 111\rangle$; slip occurs in the close-packed $\langle 111\rangle$ directions in this bcc structure. The crystallographic slip planes are the $\{110\}$ planes. The $\frac{1}{2}\langle 111\rangle$ dislocations of magnitude 2.48 Å can be seen at the center of the slip region marked by the rightmost arrow in 10(f). Surrounding this central region of red atoms are green and blue atoms with slip vectors of magnitude $\frac{1}{3}\langle 111\rangle$ and $\frac{1}{6}\langle 111\rangle$ respectively. From the front edge of the tip dislocations are emitted in four separate $\langle 111\rangle$ directions in $\{110\}$ planes.

Analysis of the local geometric configuration and potential energy of the Si atoms underneath the tip shows that there are no sub-surface dislocations generated. However, we have observed that at the depth of 15 Å some of the Si atoms have undergone a phase transformation instead, although no large-scale phase transformations have been seen at the depth considered in this investigation. Figs. 11(a)-11(b) show how the co-ordination number of some of the Si atoms changes at a depth of 15 Å. Shown are the Si atoms with coordination numbers of between 5 and 8, with the majority of these being 5-fold or 6-fold coordinated. It can be seen in Fig. 11 that as the tip slides

there is some elastic recovery behind the tip with a reduction in the over-co-ordinated atoms. The majority of the over-co-ordinated Si atoms are those that are under pressure around the tip. After the tip has passed some 5 or 6 co-ordinated atoms remain under the groove. There is no noticeable structure to the stressed region below the groove and the tip which appears only as a denser amorphised region.

4.2.2 ***Effect of constraining the indenter motion in the z-direction***

Fig. 12 shows the behaviour of the friction coefficient as a function of the horizontal displacement of the indenter on the Ag substrate at a depth of 5 Å, for the two different cases where the motion of the indenter was constrained and unconstrained in the z-direction. A slight difference is observed when the spring in the z-direction is switched on, compared to constrained motion but this effect is small. Table 4 shows that both the dynamic and the static friction coefficients were found to be only slightly higher when the tip motion was constrained in the z-direction.

4.2.3 ***Effect of temperature: 0 K versus 300 K***

The emission of dislocations in the simulations at 300 K were found to be associated with the slip events and this was also observed in our previous simulations performed at 0 K [18]. Figs. 13(a)–13(f) illustrate the dislocation emission process during the scratching simulation on the Ag substrate at a depth of 5 Å. Figs. 13(a)–13(f) should also be compared with Figs. 14(a) and 14(b). The slip event that occurred at about $t = 3.4$ ns in Fig. 14(a) shown by the sudden increase in displacement corresponds to the dislocations emitted in Figs. 13(c)–13(e). But unlike the simulations at 0 K in Ref. [18], here the dislocations are not full dislocations but rather partial dislocations and they are sometimes retracted shortly after they have been emitted, *i.e.* after the occurrence of the slip events. In fact the earlier 0 K model included damping all atoms in the system. In the new model the Nose-Hoover thermostat is attached to atoms near the boundary. It is therefore possible that the full dislocations observed in the previous model could have been an artefact of the over-damping of the system. At a vertical support displacement of 5 Å (apex indentation depth ≈ 1.25 Å) the contact pressure and scratch hardness for Ag at 0 K were found previously to be 79.2 and 38.7 GPa, respectively, whereas when the support moves through a vertical distance of 15 Å (actual indentation depth ≈ 9.86 Å) they were 26.9 and 19.6 GPa. These values are higher than the values obtained here from the simulations on Ag at 300 K. At a vertical support displacement of 5 Å the contact pressure and scratch hardness for Ag were found to be 41.9 and 35.6 GPa, respectively, whereas at a vertical support displacement of 15 Å they were 24.1 and 18.8 GPa. This is

partly because the actual indentation depths are deeper at 300 K and pressure reduces with depth. The apex indentation depths at 300 K are 2.4 and 10.7 Å for specified vertical support displacements of 5 and 15 Å, respectively.

5 Discussion and Conclusions

The trends in the variation of contact pressure and friction coefficient with depth can be simply understood by considering the form of the force-depth curves for Ag and Si during indentation. For Ag the normal force F behaves like $F \approx h^{1.2}$. The contact pressure $P \approx F/A_c$ where A_c is the cross-sectional area, given by $A_c = \frac{3}{2}\sqrt{3}(h+l)^2$ where l is the depth of the rounded tip apex from the cube corner. If l is assumed to be small ($\approx$ 3 Å in our case) then $P \approx h^{-0.8}$. Assuming that the tangential frictional force is proportional to the area A_T of the tip in contact with the surface, $A_T = \frac{9}{2}h^2$ for a perfect cube corner, then the friction coefficient $\mu \approx h^{0.8}$ increases with depth. A similar argument gives $\mu \approx h^{0.4}$ for Si and $P \approx h^{-0.4}$. Thus the basic trends in the variation of friction coefficient with depth given in table 3 can be estimated from a simple knowledge of the $F - h$ variation.

The dynamic friction coefficient, which is an average value over the length of the scratch, calculated using our current model for Ag at the depth of 15 Å is almost identical to that previously calculated with a forced motion model [23]. In addition, the value of both the dynamic and the static friction coefficients of Ag agree almost exactly with those values obtained from the simulations with the 2-spring model at 0 K [18]. Both Si and H-terminated Si were found to have higher dynamic and static friction coefficients compared to the values for the metals. However, both the dynamic and static friction coefficients of Si were higher compared to the friction coefficients for H-terminated Si, but the difference between the dynamic friction coefficient for Si and the one for H-terminated Si decreases with increasing indentation depth.

Experimental investigations have been carried out on the (100) surface of untreated Si and Al single crystals. Qualitative comparisons between the experimental measurements and the MD simulations were made where possible. We observed a qualitative agreement between the experimental and theoretical results, especially for the scratch geometry but higher contact pressures due to the small depths indented in the simulations.

The simulations also showed that for the case of the metals (Ag and Fe) stick-slip is associated with the production of dislocations in the substrate below the indenter and this observation was also made in our previous studies at 0 K [18]. Unlike the 0 K simulations, the dislocations at 300 K are not full dislocations but rather partial dislocations and they are often retracted shortly

after the occurrence of the slip events. For the case of Si, no dislocations are generated, instead some of the Si atoms undergo phase transformations, and the coordination number varies between 5 and 8, with the majority being 5-fold and 6-fold coordinated.

The constriction of the indenter motion in the lateral (z) direction was not found to have a significant influence on the dynamics of the system.

6 Acknowledgements

This work has been funded by EPSRC grants GR/R18581/01 and GR/R67699/02, a Pro-Inno project funded from the state of Brandenburg and a Royal Society joint project grant. One of the authors (DM) would like to thank the EPSRC and Loughborough University for financial support. The calculations were carried out using Loughborough University's high performance computing and visualisation facility.

References

[1] F. P. Bowden and D. Tabor *The Friction and Lubrication of Solids* (Oxford: Clarendon) (1954).

[2] E. Rabinowicz *Friction and Wear of Materials*, (John Wiley & Sons, Inc., 1965).

[3] D. Dowson, *History of Tribology*, (Longman, New York, 1979).

[4] B. N. J. Persson, *Sliding Friction, Physical Principles and Applications,* Second Edition, (Springer, 2000).

[5] B. Bhushan, *Handbook of Micro/Nano Tribology*, 2nd edition (CRC Press, Boca Raton, FL, 1999).

[6] A. L. Demirel and S. Granick *Phys. Rev. Lett.* **77**, 4330 (1996).

[7] C. M. Mate, G. M. McClelland, R. Erlandsson, and S. Chiang *Phys. Rev. Lett.* **59**, 1942 (1987).

[8] U. Landman, W. D. Luedtke, and M. W. Ribarsky, *J. Vac. Sci. Technol. A* **7**, 2829 (1989).

[9] U. Landman, W. D. Luedtke, and E. M. Ringer, *Wear* **153**, 3 (1992).

[10] M. R. Sørensen, K. W. Jacobsen and P. Stoltze *Phys. Rev. B* **53**, 2101 (1996).

[11] J. A. Harrison, C. T. White, R. J. Colton, and D. W. Brenner, *Acta Metall. Mater.* **40**, 2503 (1992).

[12] J. A. Nieminen, A. P. Sutton, and J. B. Pethica, *Wear* **153**, 3 (1992).

[13] T. Cagin, J. Che, M. N. Gardos, and A. Fijany *Nanotechnology* **10**, 278 (1999).

[14] M. Brandbyge, J. Schiøtz, M. R. Sørensen, P. Stoltze, K. W. Jacobsen, J. K. Nørskov, L. Olesen, E. Laegsgaard, I. Stensgaard and F. Besenbacher *Phys. Rev. B* **52**, 8499 (1995).

[15] S. Fujisawa, E. Kishi, Y. Sugawara, S. Morita *Phys. Rev. B* **51**, 7849 (1995).

[16] Bin Li, P. C. Clapp, J. A. Rifkin and X. M. Zhang *J. Appl. Phys.* **90**, 3090 (2001).

[17] J. Shimizu, H. Eda, M. Yoritsune and E. Ohmura *Nanotechnology* **9**, 118 (1998).

[18] D. Mulliah, S. D. Kenny and Roger Smith *Phys. Rev. B* **69**, 205407 (2004).

[19] D. Christopher, R. Smith, A. Richter *Nucl. Instr. and Meth. in Phys. Res. B* **180**, 117 (2001).

[20] D. Christopher, R. Smith, A. Richter *Nanotechnology* **12**, 372 (2001).

[21] R. Smith, D. Christopher, S. D. Kenny, A. Richter and B. Wolf *Phys. Rev. B* **67**, 245405 (2003).

[22] D. Mulliah, D. Christopher, S. D. Kenny and Roger Smith *Nucl. Instr. and Meth. in Phys. Res. B* **202**, 294 (2003).

[23] D. Mulliah, S. D. Kenny, Roger Smith and C. F. Sanz-Navarro *Nanotechnology* **15**, 2243 (2004).

[24] D. Mulliah, S. D. Kenny and Roger Smith, *Proceedings of the 11th Nordic Symposium on Tribology* – NORDTRIB 2004, Pg. 229–238 (June 2004).

[25] D. W. Brenner, *Phys. Rev. B* **42**, 9458 (1990).

[26] D. W. Brenner, *Phys. Rev. B* **46**, 1948 (1992) (correction).

[27] G. J. Ackland, G. Titchy, V. Vitek and M. W. Finnis, *Phil. Mag.* A **56**, 735 (1987).

[28] M. W. Finnis and J. E. Sinclair, *Phil. Mag.* A **50**, 145 (1984).

[29] J. P. Biersack, J. Ziegler and U. Littmack *The Stopping and Range of Ions in Solids* (Oxford: Pergamon) (1985).

[30] J. Tersoff, *Phys. Rev. B* **37**, 6991 (1988).

[31] K. Beardmore and R. Smith, *Phil. Mag.* A **74**, 1439-1466 (1996).

[32] M. V. R. Murty and H. A. Atwater, *Phys. Rev. B* **51**, 4889 (1995).

[33] S. Nosé, *J. Chem. Phys.* **81**, 511–519, (1984).

[34] W. G. Hoover, *Molecular Dynamics*, (Springer-Verlag, Berlin, 1986).

[35] R. Smith, *Atomic and Ion collisions in solids and at surfaces*, (Cambridge University Press, 1997).

[36] B. Wolf and A. Richter, *New J. Physics* **5**, 15.1-15.17 (2003).

[37] C. F. Sanz-Navarro , S. D. Kenny and Roger Smith *Nanotechnology* **15**, 692 (2004).

[38] A. Richter, B. Wolf and J. J. BelBruno, *Trans. Tech. Publications Solid State Phenomena* **95-96**, 519-524 (2004).

[39] D. F. Bahr, D. E. Wilson and D. A. Crowson, *J. Mater. Res.* **14**, 2269 (1999).

[40] V. Blank, M. Popov, G. Pivovarov, N. Lvova, K. Gogolinsky and V. Reshetov, *Diamond Relat. Mater.*, **7**, 427 (1998).

[41] O. Rodríguez de la Fuente, J. A. Zimmerman, M. A. González, J. de la Figuera, J. C. Hamilton, Woei Wu Pai and J. M. Rojo *Phys. Rev. Lett.* **88**, 036101 (2002).

[42] D. Hull and D. J. Bacon, *Introduction to Dislocations*, 3rd Edition, (Oxford: Pergamon, 1984).

Table 1
Table showing the substrate sizes when employing Ag, Fe, Si and H-terminated Si as substrates at support depths of 5 and 15 Å. This is not the same as the actual indentation depth due to compression of both the spring and tip. The tip compression varies from about 1 Å for Si at the shallow depth to nearly 2 Å for Fe

Substrate	Dimensions of substrate ($Å^3$)	Number of substrate atoms
Ag	$180 \times 42 \times 122$	54,000
Fe	$180 \times 42 \times 102$	66,960
Si	$180 \times 42 \times 102$	43,520
H-terminated Si	$180 \times 42 \times 102$	44,880

Table 2
Results from the MD simulations, employing Ag, Fe, Si and H-terminated Si as substrates at support indentation depths of 5 and 15 Å.

Substrate	Apex indentation depth (Å)	Wear debris (No. of ad atoms)	Contact pressure (GPa)	Scratch hardness (GPa)
Support Indentation Depth of 5 Å				
Ag	2.4	89	41.9	35.6
Fe	1.0	62	144.5	68.0
Si	2.9	42	23.7	19.3
H-terminated Si	2.9	18	23.0	18.7
Support Indentation Depth of 15 Å				
Ag	10.7	792	24.1	18.8
Fe	8.8	589	50.3	34.6
Si	10.4	248	20.9	17.2
H-terminated Si	10.7	220	18.6	15.3

Table 3
Friction coefficients and pile-up height for support depths of 5 and 15 Å.

Substrate	Normal force (nN)	Frictional force (nN)	Dynamic friction coefficient	Static friction coefficient	Height of pile-up (Å)
Support Depth of 5 Å					
Ag	36.1	8.2	0.23	0.31	3.8
Fe	54.2	8.1	0.12	0.19	1.0
Si	21.7	44.0	1.51	2.66	4.1
H-terminated Si	22.5	25.7	1.08	1.69	2.6
Support Depth of 15 Å					
Ag	106.3	43.2	0.37	0.51	9.0
Fe	160.9	65.0	0.32	0.45	8.9
Si	98.1	132.3	1.35	–	8.0
H-terminated Si	90.6	115.9	0.96	1.38	7.1

Table 4
Results from the MD simulations employing Ag substrate at an indentation depth of 5 Å, for the case when the motion of the indenter is both constrained and unconstrained in the z-direction.

z-spring	Normal force (nN)	Frictional force (nN)	Dynamic friction coefficient	Static friction coefficient
ON	36.1	8.2	0.23	0.31
OFF	35.0	9.8	0.28	0.37

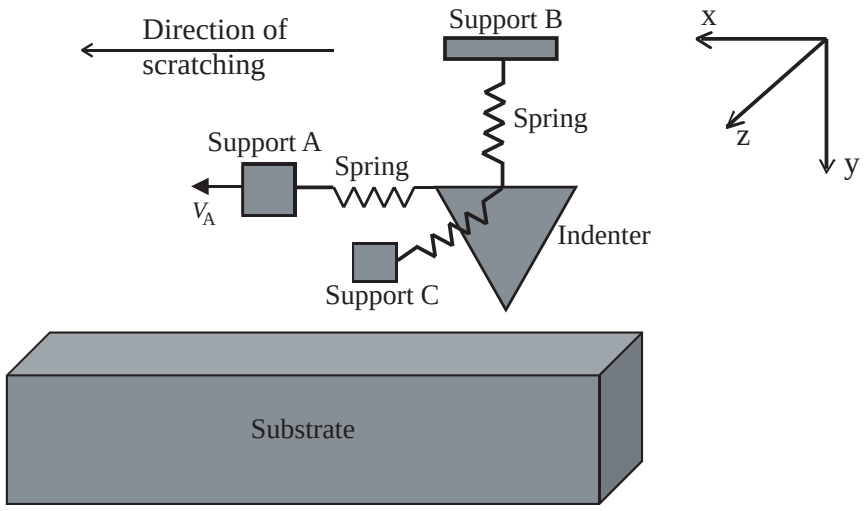

Fig. 1. Diagrammatic representation of the model used to simulate the stick-slip friction mechanism. The indenter is attached to three springs in the horizontal (x), vertical (y), and lateral (z) directions. The horizontal, vertical and lateral springs are attached to support blocks A, B and C, respectively.

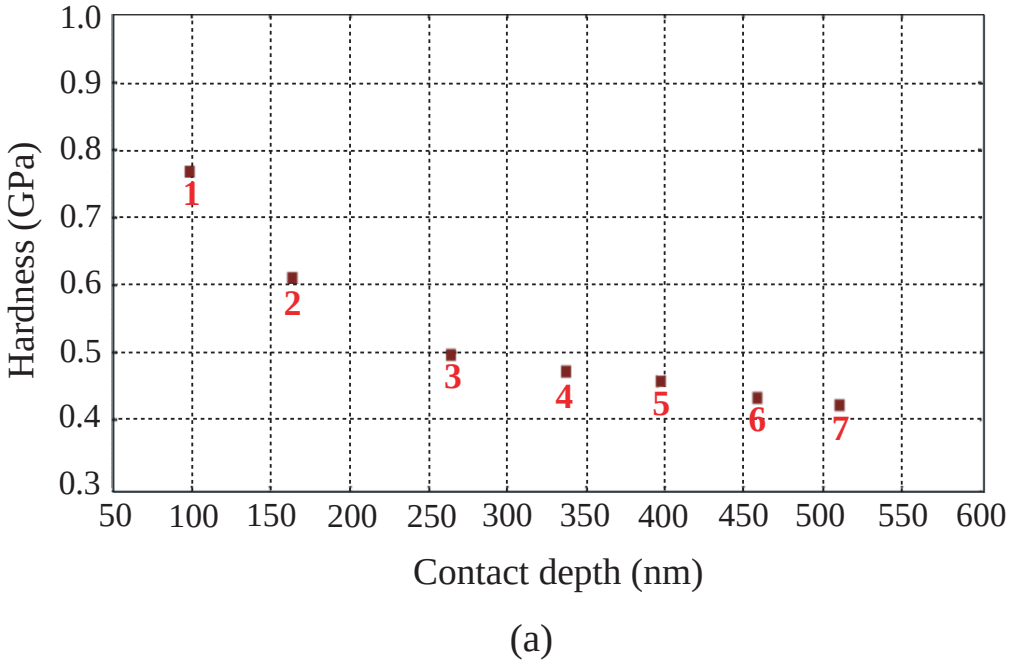

(a)

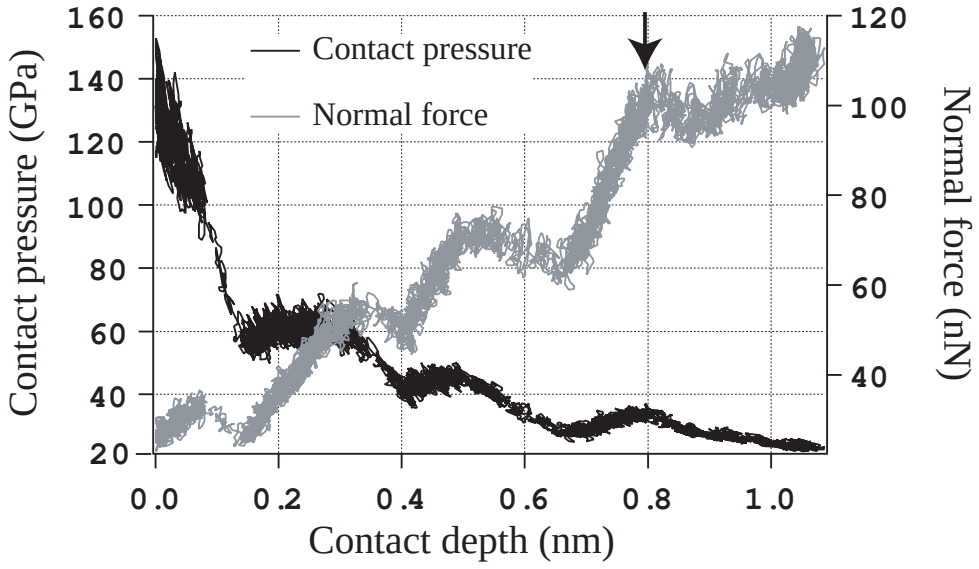

(b)

Fig. 2. (a) Graph showing the dependence of the contact pressure on the contact depth, from the multicycling nanoindentation experiment on single crystalline Al. (b) The contact pressure as a function of the penetration depth from the MD simulation on Ag at a depth of 15 Å. The arrow in (b) marks the point on the force curve corresponding to the emission of the dislocation in Fig. 3(b), at the point where the contact pressure and force are near to a local maximum.

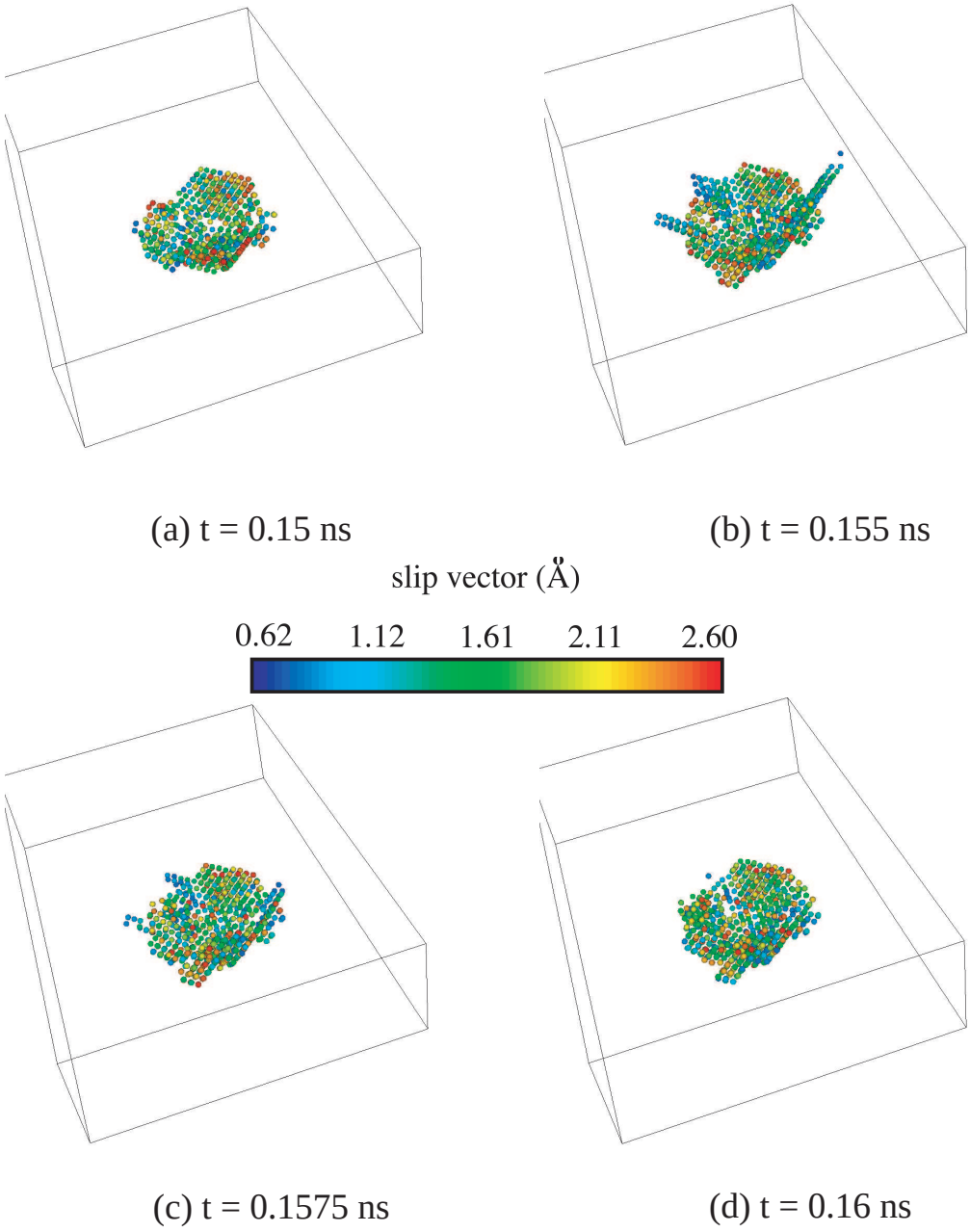

Fig. 3. (Colour online) Images of the atomic displacements underneath the tip during indentation of Ag. The displaced atoms are represented as spheres coloured according to the amount of slip. Figure (b) where the dislocations are emittted, corresponds to a depth shown by the arrow in the Fig. 2(b).

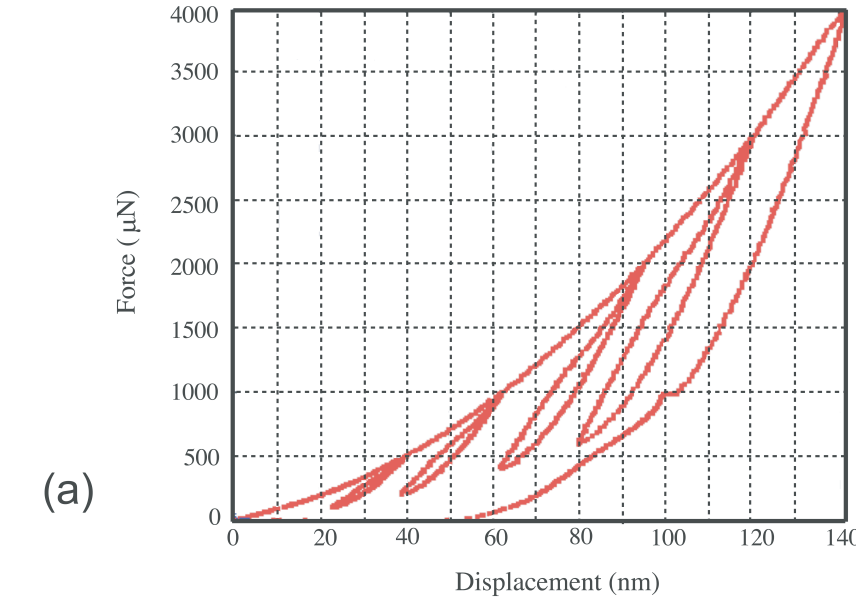

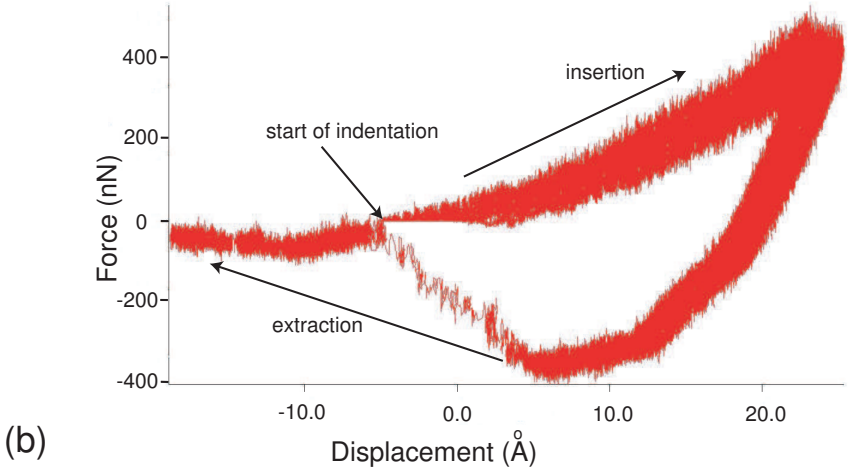

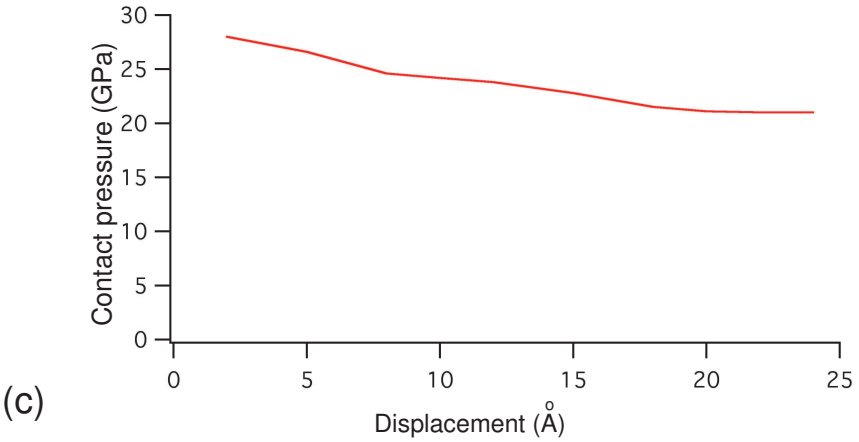

Fig. 4. (a) Force-displacement curve for the indentation experiment on untreated Si(100) surface for a multi-indent showing the unloading-reloading hysteresis loops; (b) The force-displacement curve from the simulations. (c) The contact pressure as a function of depth from the simulations; In (c) the average line is drawn as the curve in (b) oscillates due to the attached spring. Note the strong pull-off force in (b).

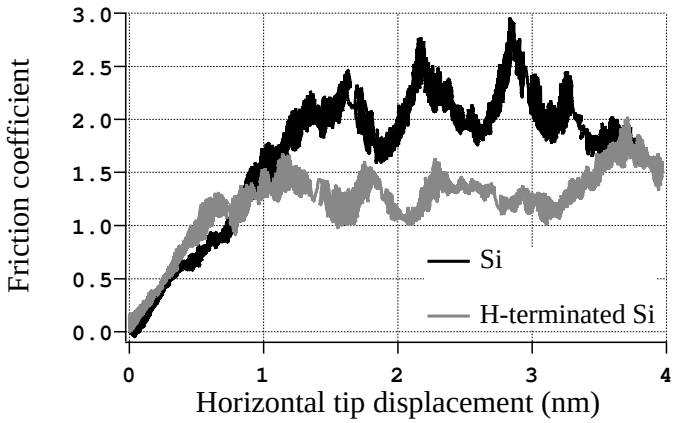

(a)

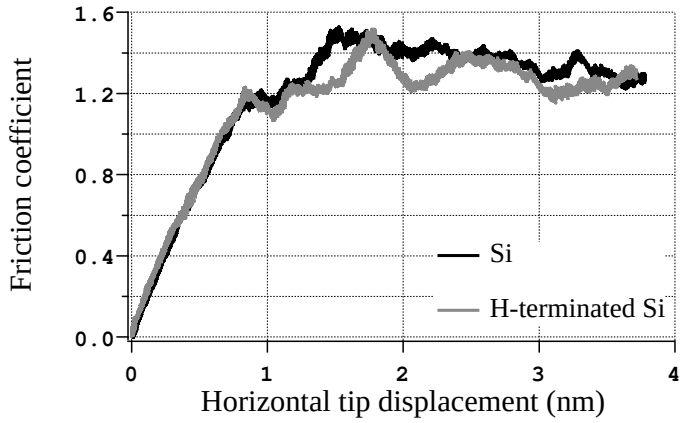

(b)

Fig. 5. Plots of the friction coefficient as a function of the horizontal displacement of the indenter during the scratching simulation, for both Si and H-terminated Si substrates at depths of (a) 5 Å and (b) 15 Å.

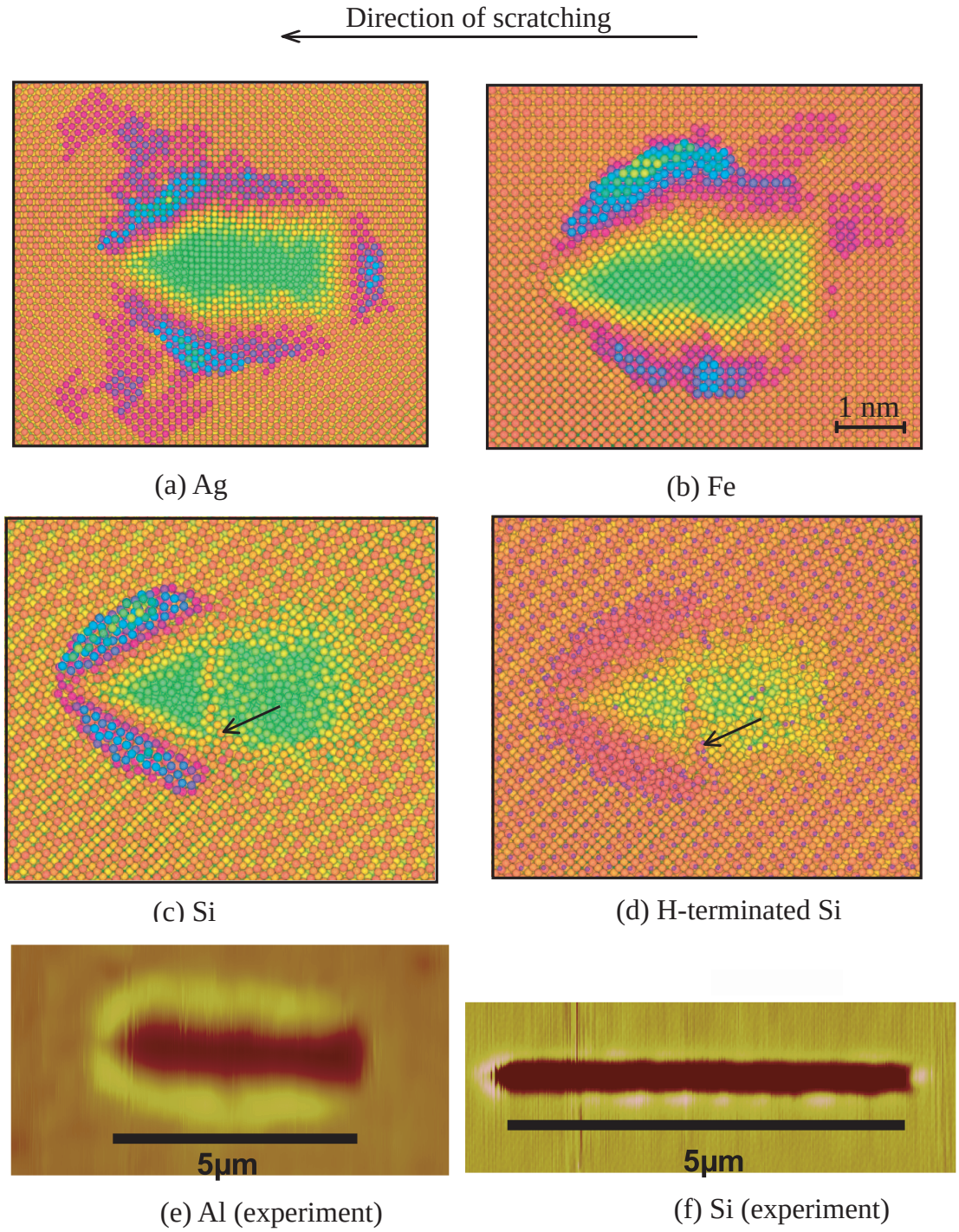

Fig. 6. (Colour online) Top view of the substrate showing the surface damage at the end of the scratching simulation, for (a) Ag, (b) Fe, (c) Si and (d) H-terminated Si, substrates at an indentation support depth of 15 Å; (e) SFM image of Al (100) after scratching with a normal force of 250 μN; (f) SFM image of Si (100) after scratching with a normal force of 1000 μN In the simulations, the atoms are coloured on depth, where the spheres around the edge of the hole represent piled up atoms on the surface and the orange atoms represent the surface atoms. The arrows in (c) and (d) show the line of Si atoms attached to the rear of the indenter during adhesion and dragged behind the tip during the scratching process. The experimental micrographs (e) and (f) show similar geometric patterns of the pile-up as in (a) and (c).

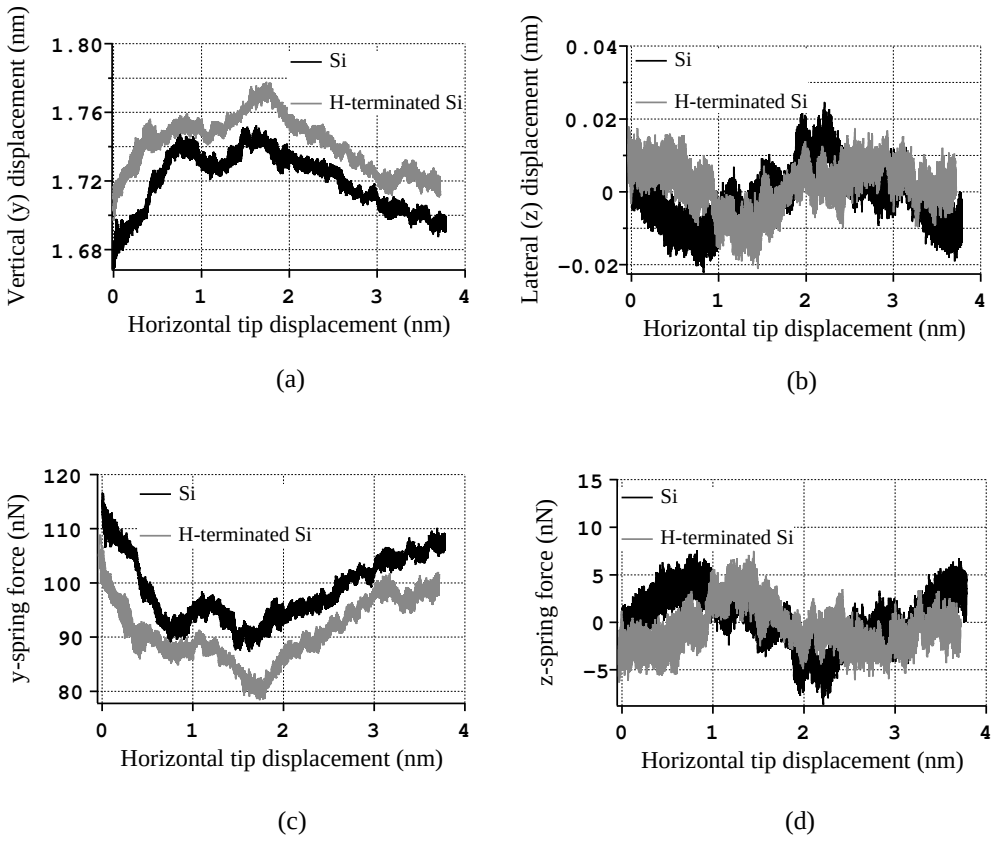

Fig. 7. Figure showing the plot of the (a) vertical (y) displacement of the indenter, (b) lateral (z) displacement of the indenter, (c) spring force in the y-direction and (d) spring force in the z-direction, as a function of the horizontal displacement of the tip during the scratching simulation, for both Si and H-terminated Si substrates at a depth of 15 Å.

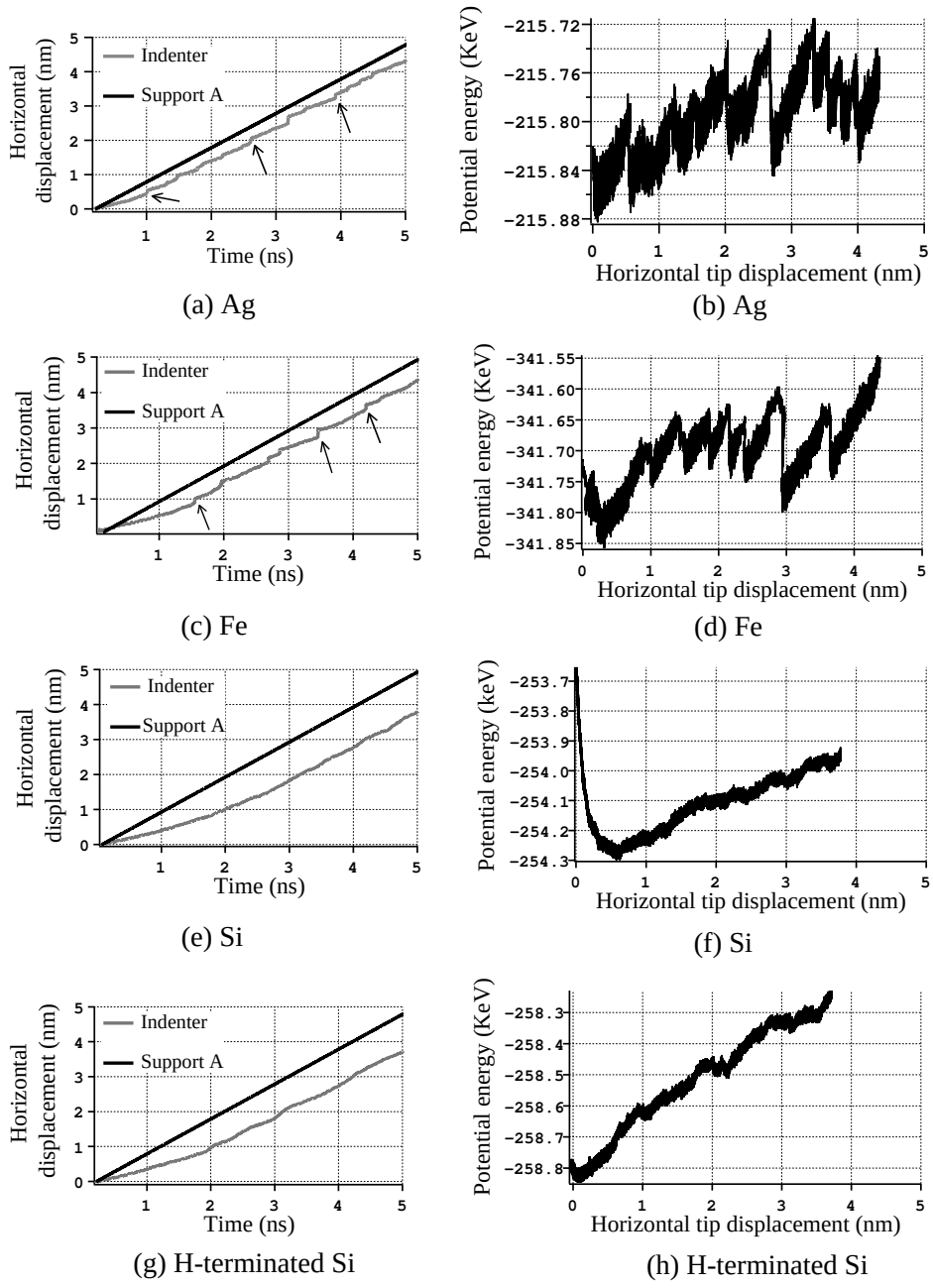

Fig. 8. Figures (a), (c), (e) and (g) show the plot of the horizontal displacement of the indenter and the support A, when employing Ag, Fe, Si and H-terminated Si as substrate, respectively. The arrows point out the occurrence of the slip events. Figures (b), (d), (f) and (h) show the plot of the potential energy of the system against the horizontal displacement of the indenter when employing Ag, Fe, Si and H-terminated Si as substrate, respectively. The plots are from the simulations performed at a depth of 15 Å.

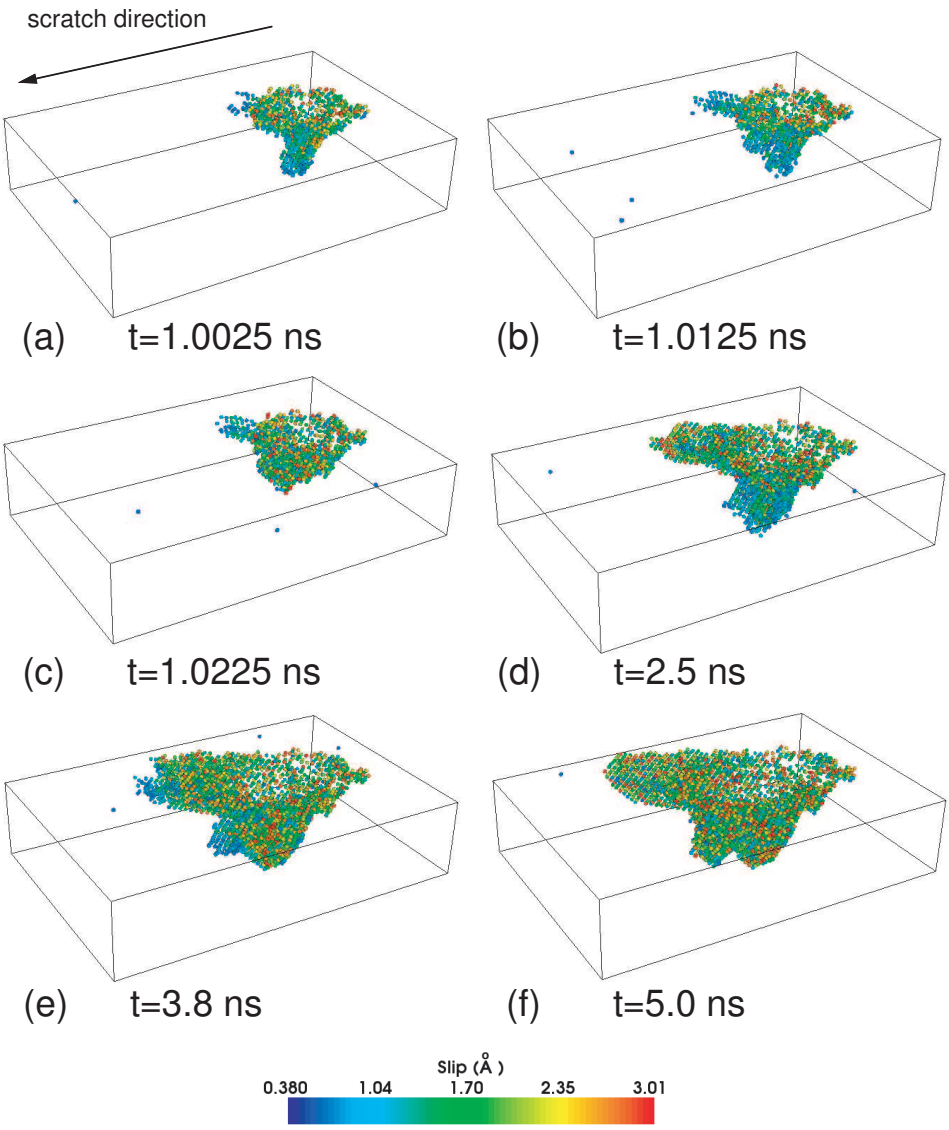

Fig. 9. (Colour online) Figures showing the emission of dislocations underneath the scratch groove during the scratching simulation on the silver substrate, at the depth of 15 Å. The figures are coloured according to the modulus of the slip vector for Ag given in the key. The box size is 18.3 nm x 4 nm x 12.2 nm.

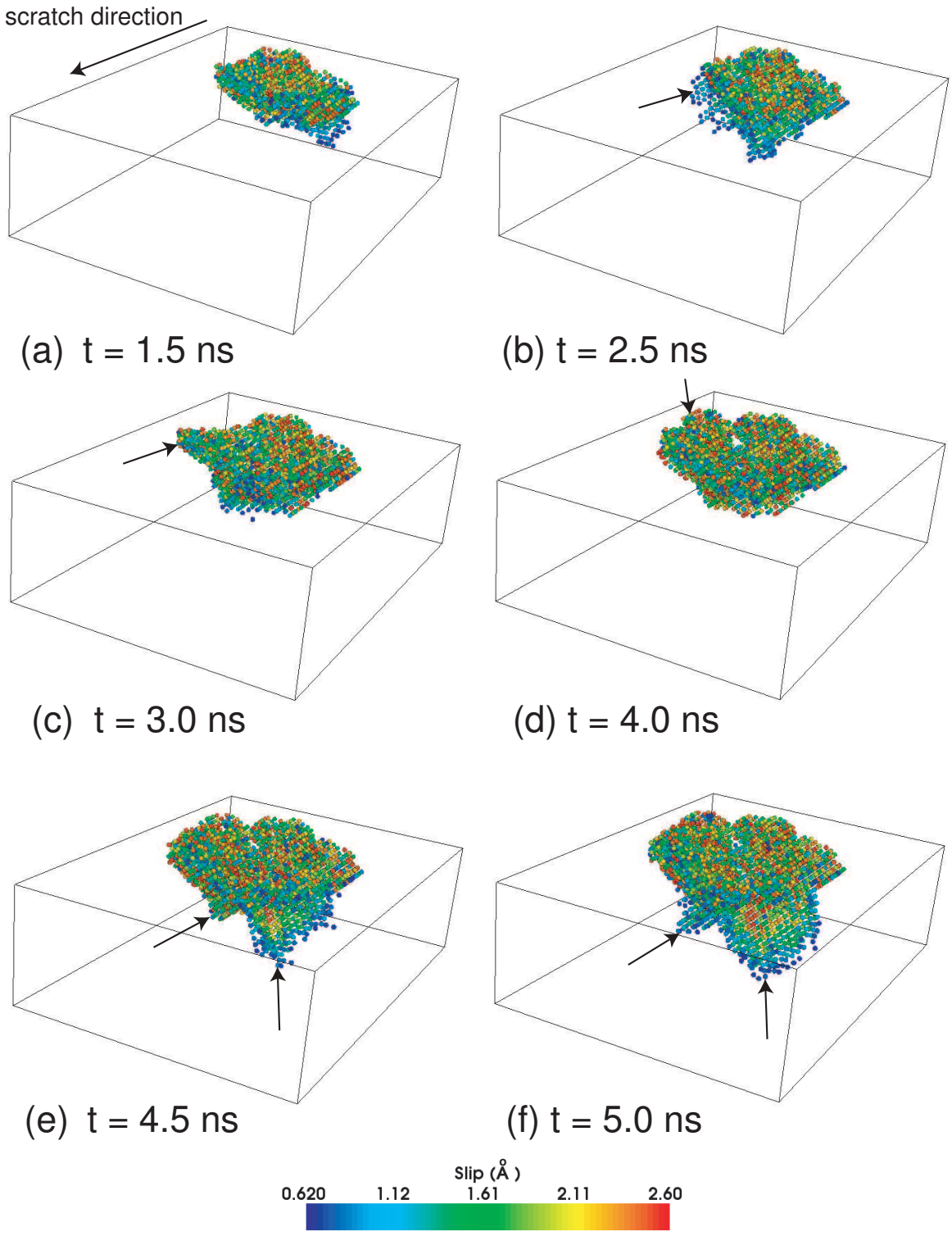

Fig. 10. (Colour online) Figures showing the top view of the subsurface damage underneath the scratch groove in the Fe substrate during the scratching simulation at a depth of 10 Å. The atoms are coloured according to the modulus of the slip vector for Fe given in the key and the arrows and circle point out the emission of dislocations. The box size is 13.7 nm x 4.2 nm x 10.3 nm.

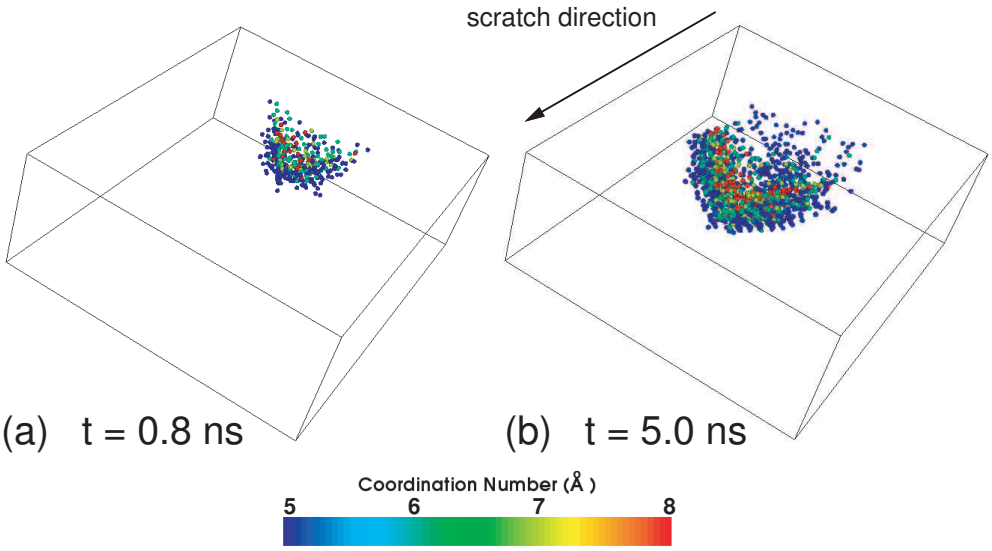

Fig. 11. (Colour online) Figures showing the Si atoms that have undergone phase transformations during the indentation and scratching simulations, at a depth of 15 Å. The atoms are coloured according to the coordination number; (a) shortly after the start of the scratch and (b) at the end of the simulation. Note the reduction in over-co-ordinated atoms after the passage of the tip. The box dimensions are 13.4 nm x 4.3 nm x 10.8 nm.

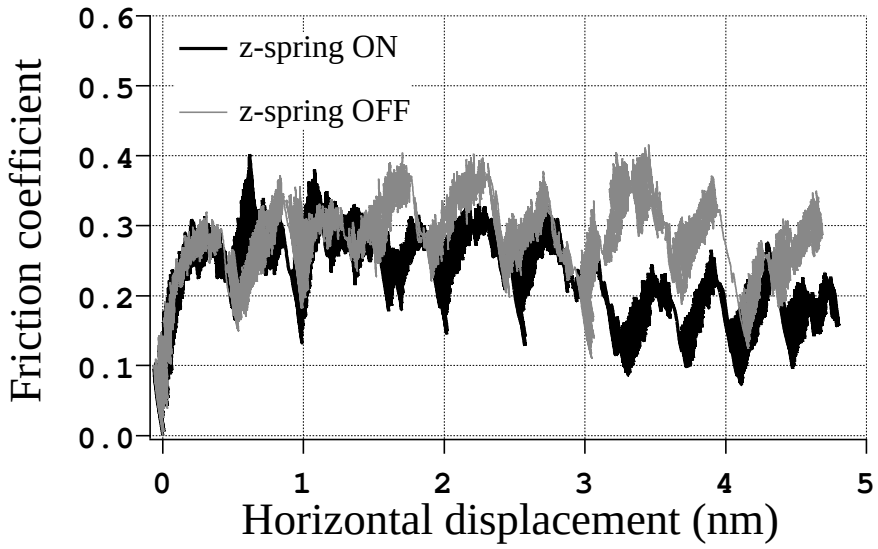

Fig. 12. Figure showing the plot of the friction coefficient against the horizontal displacement of the indenter on the silver substrate during the scratching simulation, at a depth of 5 Å, for the two cases where the spring in the z-direction was switched on and off.

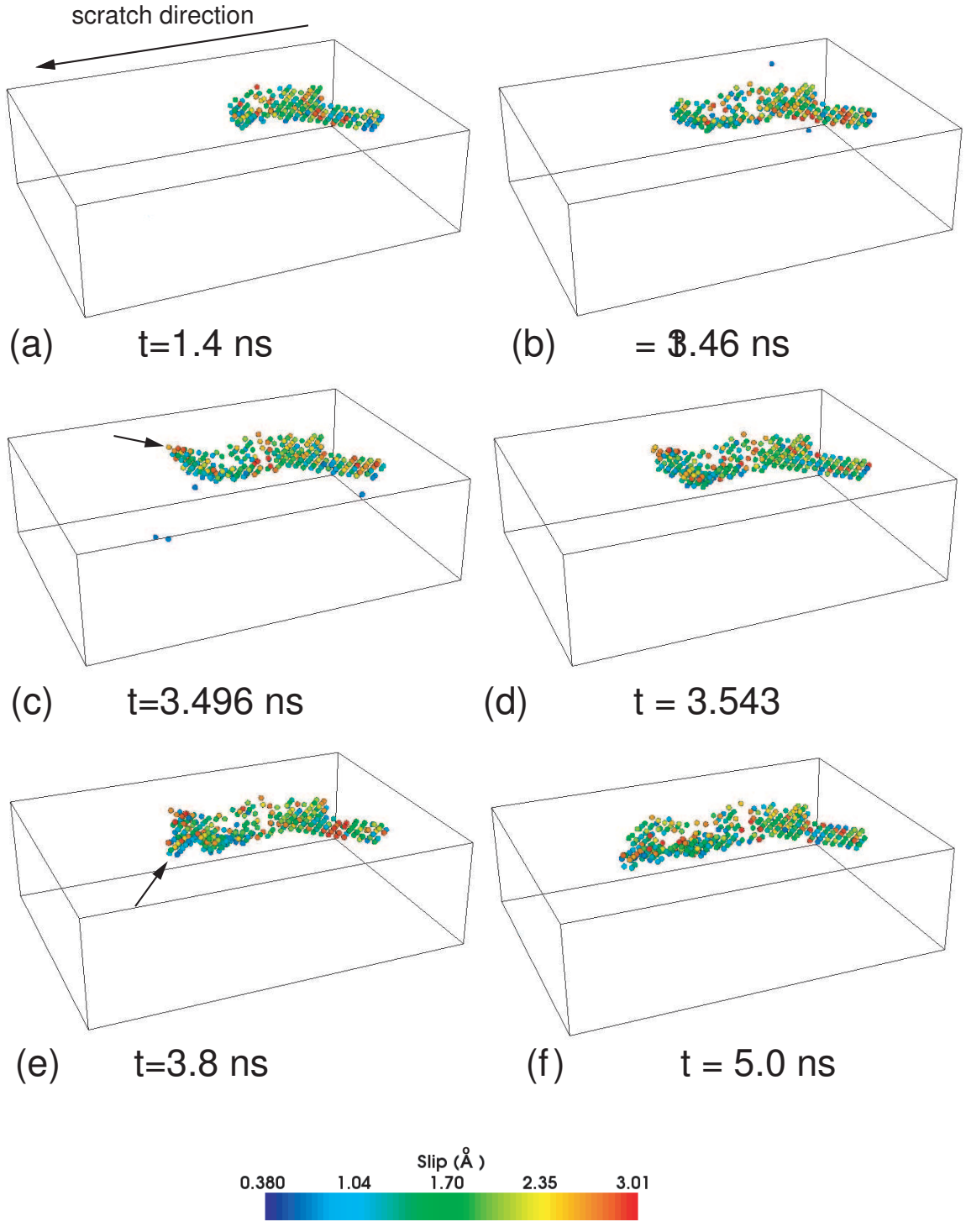

Fig. 13. (Colour online) Figures showing the emission of dislocations underneath the scratch groove in the silver substrate, for a support displacement of 5 Å. The atoms are coloured according to the modulus of the slip vector for Ag given in the key and the arrows point out the emission of the partial dislocations. The box size is 13.9 nm x 4 nm x 10.4 nm.

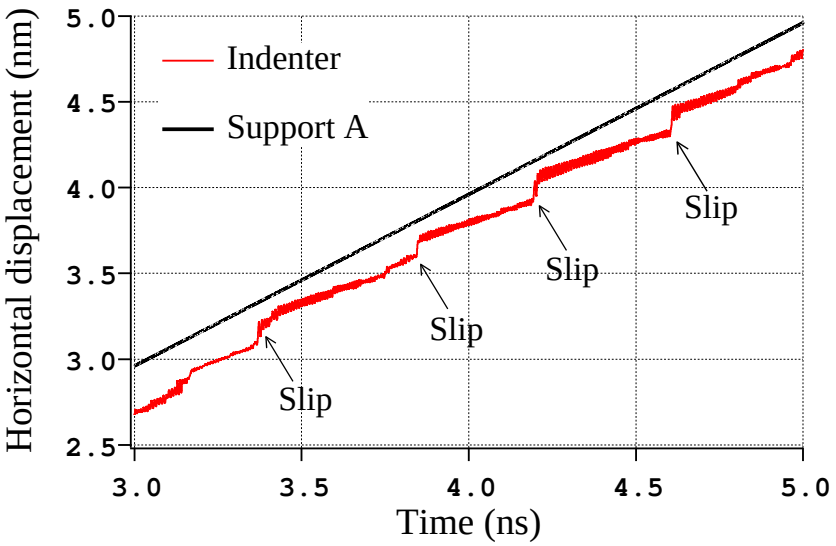

(a)

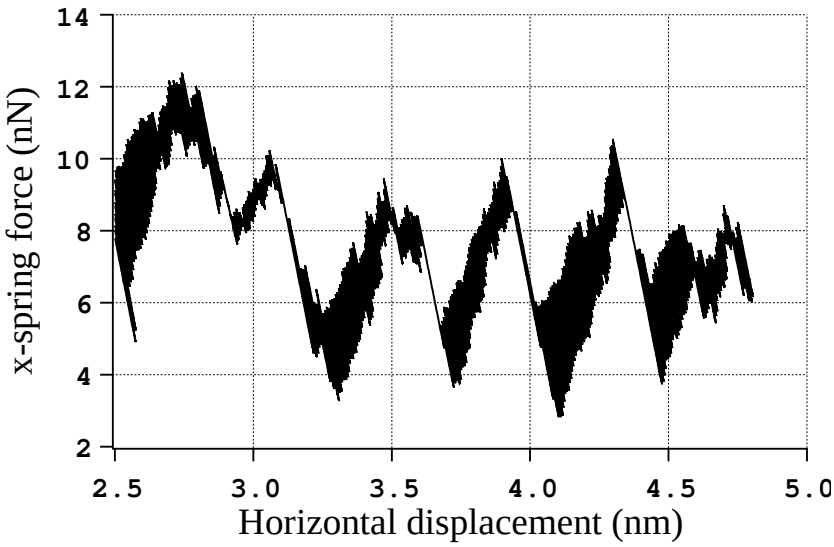

(b)

Fig. 14. Plot of (a) the horizontal displacement of both the indenter and the horizontal support A, and (b) the horizontal spring force of the indenter, during the scratching simulation on the Ag substrate, at a depth of 5 Å. The arrows in (a) indicate the occurrence of the slip events.